arXiv:1505.07743v1 [astro-ph.SR] 28 May 2015

# A COMPACT CONCENTRATION OF LARGE GRAINS IN THE HD 142527 PROTOPLANETARY DUST TRAP

Simon Casassus[1,2], Chris Wright[3], Sebastian Marino[1,2], Sarah T. Maddison[4], Al Wootten[5], Pablo Roman[6,2], Sebastian Pérez[1,2], Paola Pinilla[7], Mark Wyatt[8], Victor Moral[6,2], Francois Ménard[9], Valentin Christiaens[1,2], Lucas Cieza[10], Gerrit van der Plas[1,2]

*Draft version May 29, 2015*

## ABSTRACT

A pathway to the formation of planetesimals, and eventually giant planets, may occur in concentrations of dust grains trapped in pressure maxima. Dramatic crescent-shaped dust concentrations have been seen in recent radio images at sub-mm wavelengths. These disk asymmetries could represent the initial phases of planet formation in the dust trap scenario, provided that grain sizes are spatially segregated. A testable prediction of azimuthal dust trapping is that progressively larger grains should be more sharply confined and furthermore the trapped grains should follow a distribution that is markedly different from the gas. However, gas tracers such as CO and the infrared emission from small grains are both very optically thick where the submm continuum originates, so observations have been unable to test the trapping predictions or to identify compact concentrations of larger grains required for planet formation by core-accretion. Here we report multifrequency observations of HD 142527, from 34 GHz to 700 GHz, that reveal a compact concentration of ∼cm-sized grains, with a few Earth masses, embedded in a large-scale crescent of ∼mm-sized particles. The emission peaks at wavelengths shorter than ∼1 mm are optically thick and trace the temperature structure resulting from shadows cast by the inner regions. Given this temperature structure, we infer that the largest dust grains are concentrated in the 34 GHz clump. We conclude that dust trapping is efficient for approximately cm-sized grains and leads to enhanced concentrations, while the smaller grains largely reflect the gas distribution.

*Subject headings:* Protoplanetary disks — Planet-disk interactions — Stars: individual: (HD 142527)

## 1. INTRODUCTION

Giant planet formation occurs in the first few million years following stellar birth, while the parent protoplanetary disk is still gas-rich (Zuckerman et al. 1995). However, the classical debate on the formation mechanism, if envelope accretion onto a rocky core, i.e. core-accretion (Pollack et al. 1996), or gravitational instability (Kuiper 1951), is stalled without observations. The pathway to giant planet formation determines the initial configuration and compositions of the product planetary systems. Current trends in theory contemplate a variety of formation scenarios, notably second-generation core-accretion at large radii following the formation of a giant closer-in (Ayliffe et al. 2012; Sándor et al. 2011). Models predict that young giant protoplanets carve a deep gap in the dust component of protoplanetary disks, and a shallower gap in the gas (Paardekooper & Mellema 2006; Fouchet et al. 2010). The clearing of the protoplanetary gap is thought to underlie the class of 'transition' disks. A local pressure maximum develops at the outer edge of the gap, that can trap and pile-up the larger grains (Zhu & Stone 2014), which would otherwise rapidly migrate inwards due to aerodynamic drag (Weidenschilling 1977) (as in the so-called 'meter-size barrier', which at 50–100 AU corresponds to mm-sized particles). Local pressure maxima could also occur in lopsided disks with a stellar offset (Mittal & Chiang 2015). Whichever is origin, the development of a local pressure maximum may promote the pile-up and growth of dust grains, and the formation of large dust clumps that could eventually collapse in planetary cores (Ayliffe et al. 2012; Lyra et al. 2009; Sándor et al. 2011).

Recent observational progress brought by the Atacama Large Millimeter Array (ALMA) fits in the scenario of second-generation planet-formation at large stellocentric radii. The observational identification of so-called dust traps, in the form of concentrations of mm-sized dust (Casassus et al. 2013; van der Marel et al. 2013) in the outer regions of transition disks, suggests that azimuthal dust trapping may occur. An important prediction of this scenario is that progressively larger grains should be more sharply confined (Birnstiel et al. 2013; Lyra & Lin 2013), possibly leading to the formation of boulders and planetesimals. Another consequence is that the larger dust grains should have a distribution that is markedly different from the gas. Observed contrast ratios of 30 to 100 between extrema in the sub-mm continuumm (at coarse angular resolutions) would seem too large to re-

[1] Departamento de Astronomía, Universidad de Chile, Casilla 36-D, Santiago, Chile
[2] Millennium Nucleus "Protoplanetary Disks", Chile
[3] School of Physical, Environmental and Mathematical Sciences, UNSW Canberra, PO Box 7916, Canberra BC 2610, Australia
[4] Centre for Astrophysics & Supercomputing, Swinburne University of Technology, PO Box 218, Hawthorn, VIC 3122, Australia
[5] National Radio Astronomy Observatory, 520 Edgemont Road, Charlottesville, VA 22903-2475, USA
[6] Center for Mathematical Modeling, Universidad de Chile, Av. Blanco Encalada 2120 Piso 7, Santiago, Chile
[7] Leiden Observatory, Leiden University, P.O. Box 9513, 2300RA Leiden, The Netherlands
[8] Institute of Astronomy, University of Cambridge, Madingley Road, Cambridge CB3 0HA, United Kingdom
[9] UMI-FCA, CNRS / INSU France (UMI 3386), at Departamento de Astronomía, Universidad de Chile, Santiago, Chile
[10] Facultad de Ingeniera, Universidad Diego Portales, Av. Ejrcito 441, Santiago, Chile

flect an equally lopsided gas distribution. However, a theoretical question remains as to the impact of enhanced cooling in the dust trap on the physical conditions. In observational terms, the use of gas tracers such as CO or the infrared (IR) emission from small grains are both very optically thick where the ALMA thermal continuum originates, so that the previous observations (Casassus et al. 2013; van der Marel et al. 2013; Pérez et al. 2014) could not test the trapping predictions. For instance, in IRS 48 the outer ring is optically thick in the mid-IR emission (Bruderer et al. 2014, their Sec. 4.1), as is CO(6-5) whose azimuthal structure is largely determined by foreground absorption.

Since emission at a given wavelength is dominated by grains of a matching size, multi-wavelength radio observations can confirm if the crescent-shaped continua seen in transition disks are indeed due to the dust trap phenomenon. In this work we compare new ALMA high-frequency radio continuum observations of HD 142527, obtained at 700 GHz (ALMA band 9; wavelengths of ∼0.43 mm, described in Appendix, Sec. A.1), with resolved images at 34 GHz (8.8 mm) acquired at the Australia Telescope Compact Array (ATCA, see Sec. A.2). In Section 2 we show that the optical depths are of order ∼1 at 345 GHz, so that the sub-mm spectral trends observed with ALMA correspond to optical depths effects rather than to dust trapping. In Sec. 3 we explain that the ATCA observations reveal a compact clump at 34 GHz embedded in the sub-mm crescent, which is reflected by an opacity spectral index corresponding to larger grains, as expected in the dust trapping scenario. In Sec. 4 we discuss the observational results in terms of radiative transfer predictions based on a parametric dust trap mode. Sec. 5 summarises our results.

## 2. AN OPTICALLY THICK SUB-MM CONTINUUM

The ALMA band 9 continuum (Figure 1) has a morphology that is intermediate between the broken ring seen in the thermal IR at 18 $\mu$m (Fujiwara et al. 2006; Verhoeff et al. 2011) and the 345 GHz crescent seen in ALMA band 7 (Casassus et al. 2013). The maximum radial width of the crescent, measured at half-maximum, is about 0.6″, so is resolved with a beam size of 0.25″.

A traditional means to quantify the spectral variations as a function of position is the spectral index map $\alpha(\vec{x})$, with a power-law parameterisation of the specific intensity $I_\nu = I_{\nu\circ}(\nu/\nu_\circ)^{\alpha(\vec{x})}$. We find that the spectral index between 345 GHz and 700 GHz, $\alpha_{345}^{700}$, as well as the slope of the spectrum across the 0.13 GHz frequency lever within ALMA band 7, $\alpha_{345}$, both anti-correlate with the continuum crescent (see Sec. A.6), meaning that the azimuthal extension is greater at shorter wavelength. However, while the band 7 and band 9 continua peak between 10h and 11h as a function of azimuth along the outer ring, the spectral index maps exhibit a common minimum at ∼1h, i.e. at the northern ansa of the ring. This coincidence is indicative of a projection effect, as in limb-brightening: if column densities are greater at 1h, the increased optical depths will result in flatter spectra.

The spectral variations inferred from the multi frequency morphological trends can be cast into sky maps for the optical depth $\tau(\vec{x}) = \tau_\circ(\vec{x}) \times (\nu/\nu_\circ)^{\beta_s(\vec{x})}$ and line-of-sight temperature $T_s(\vec{x})$, as a function of angular
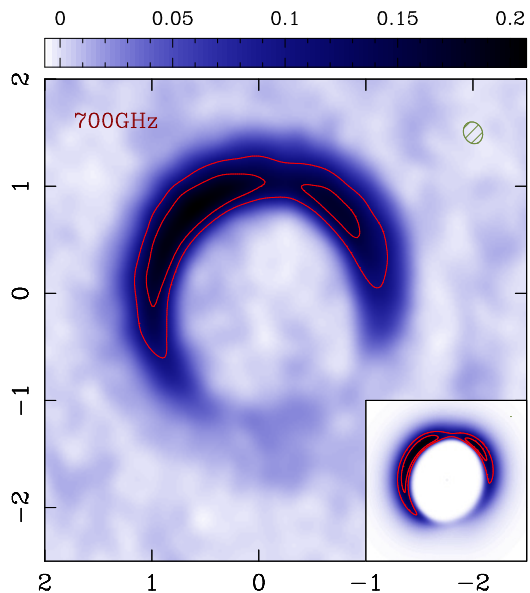


**Figure 1.** ALMA band 9 observations of HD 142527, and comparison with synthetic predictions. $x-$ and $y-$ axes indicate angular offset in arcsec along right-ascension (RA) and declination (Dec) relative to the stellar position, at the origin of coordinates. The color scale shows a restored image of the ALMA band 9 at 700 GHz, with contours at 0.5 and 0.75 times the peak intensity. The wedge indicates specific intensity in Jy beam$^{-1}$, with a beam of 0.21×0.17 arcsec (the beam ellipse is shown on the upper right corner). The inset shows emergent intensities predicted from the dust trap model (see Sec. 4), including the impact on grain temperatures due to shadowing from a tilted inner disk. Contours are at 0.5 and 0.75 times the peak, no smoothing has been applied. The side of the inset corresponds to 3.5 arcsec.

position $\vec{x}$. We fit the observations with the intensities emergent from a uniform slab (hereafter 'grey-body', see Sec. A.5 and Sec. E),

$$I_\nu^m(\vec{x}) = B_\nu(T_s(\vec{x})) \left[1 - \exp(-\tau(\vec{x}))\right].$$

The inferred temperature field approximates the opacity-weighted average temperature along the line of sight (see Sec. 4.1 for a discussion of biases). In synthesis, as explained in Sec. E) and illustrated in Fig. 8, the crescent reaches optical depths close to 1 at 345 GHz, even in a rather coarse beam (which dilutes the signal). The optical depth maximum is coincident with the location where the sub-mm spectral index ($\alpha_{345}^{700}$ and $\alpha_{345}$) is minimum, thus in agreement with an interpretation of the spectral index variations in terms of optical depth effects, rather than genuine variations of the underlying dust grain populations. Another consequence of the high submm optical depths is that the double-peaked crescent morphology, best seen in band 9, reflects structure in the temperature field rather than in the density field inside the dust trap. The local band 9 emission maxima, at 10.5h and 1.5h, are separated by a minimum in temperature at 0.5h.

## 3. ATCA/ALMA MULTI-FREQUENCY RESULTS

### 3.1. A 34 GHz clump embedded in the sub-mm crescent

Resolved ATCA observations of HD 142527 in the optically thin 34 GHz continuum reveal structure inside the sub-mm-opaque crescent, as shown in Fig. 2 (see also Fig. 3). The lower levels at 34 GHz follow the Rayleigh-Jeans extension of the hotter dust seen in ALMA band 9. However, the peak signal stems from clumpy emission at ~11.5h and a longer arc at 1h to 2h. Both regions coincide fairly closely with molecular decrements (Sec. C). Given the thermal noise in the field, the 11.5 h clump is significant at $10\sigma$, and it is robust against $uv-$filtering biases. To test for interferometer filtering artefacts, we ran Monte-Carlo simulations of ATCA observations on a deconvolved model image of the band 7 data (see Sec. B), thus bringing the multi-frequency data to an approximately common Fourier basis. Fig. 2 shows that the ATCA clump stands out compared to the filtered ALMA maps.

The peak 34 GHz intensity at 11.5h reaches $147\mu$Jy beam$^{-1}$, with a $0.64'' \times 0.30''$ beam, and has an equivalent brightness temperature of only 0.5 K, hence the signal is optically thin (or else it is beam-diluted). For the fiducial density of water, and for a single grain size of 1 cm with a circular cross section, at 20 K, we find that the observed flux density from the unresolved 11.5h clump corresponds to >7.4 M$_\oplus$ of dust. The inequality accounts for the possibility of locking more mass in grains of different sizes that do not emit appreciably at 34 GHz.

A compact signal coincident with the stellar position is conspicuous in the ATCA map. Its spectral index at ATCA frequencies is $\alpha_{20}^{45} = 1.0 \pm 0.2$, which extrapolates to the level of the faint circumstellar signal seen in ALMA band 7 (Casassus et al. 2013; Fukagawa et al. 2013). These spectral index values are consistent with free-free emission associated with a stellar wind, or with stellar accretion.

## 3.2. *Evidence for dust trapping*

In another application of the grey-body diagnostics, we computed the optical depth and opacity index ($\beta_S$) maps corresponding to the ATCA and ALMA datasets shown in Fig. 2a. The resulting optical depth map shown in Fig. 2c confirms the levels at 345 GHz inferred from the ALMA band 7 and band 9 comparison. The ATCA clump at 11.5h translates to a minimum in $\beta_S(\vec{x})$ (Fig. 2d). This is an indication that dust grains in this clump are larger than in the rest of the crescent. As summarised in Fig. 9, the variations in $\beta_S$ are significant at ~7 $\sigma$.

## 4. PREDICTIONS BASED ON A SYNTHETIC DUST TRAP MODEL

### 4.1. *Biases of the grey-body diagnostics*

The grey-body line-of-sight diagnostic is based on 2-dimensional sky maps for $\beta_S(\vec{x})$ and $T_S(\vec{x})$, while the actual physical conditions are 3-dimensional. Since the crescent is optically thick in band 9, the temperature is mainly set by the higher frequencies, and probably overestimates the temperature in regions closer to the midplane. Hence the actual optical depths could be higher than inferred from grey-body diagnostics. In order to assess biases and test the dust trap interpretation, we applied the same observational diagnostic, based on the

grey-body fits, to synthetic radiative transfer predictions of a parametrised dust trap model meant to approximate the phenomenon observed in HD 142527. The synthetic model was implemented in RADMC3D (Dullemond et al. 2015) (Methods), and centers the dust trap at 11.5h. At the native resolution of the radiative transfer, the grey-body optical depth map reproduces the input optical depths very closely. However, both optical depth and temperatures are biased downwards by ~50% after filtering by the ATCA response. The location of the minimum in the grey-body opacity index, $\beta_S(\vec{x})$, coincides with the input dust trap, which is fairly optically thick in band 7. However the optical depths in the synthetic trap are not high enough to result in the observed deep molecular decrements - their properties could be reproduced by prescribing gas temperatures cooler than the dust (Sec. C). In particular the existence of decrements in CO(2-1) (Perez et al. 2015), so at frequencies with lower optical depths, suggests that there is ample room for other effects. The decrements may also correspond to structural features of the disk, i.e. shadowing in lower scale heights under the 34 GHz clumps, due to midplanes cooler than in the rest of the outer disk at the same stellocentric radius. A mechanism for such a local 'pinching' of the outer disk may be found in the dust trap scenario. In radiative equilibrium the larger grains tend to be cooler, so that hydrostatic scale heights will be lower under the dust trap. The shadowed CO is cooler, or possibly frozen out and condensed onto grain surfaces.

### 4.2. *Temperature decrement due to shadowing on the outer-ring*

The temperature structure inferred from the band 9 observations are readily explained by the model, which includes a tilted inner disk within 20 AU, as implied by the shadows in scattered light cast on the outer disk (Marino et al. 2015). Fig. 1 shows that the predicted emergent intensities in band 9 are double-peaked, much like the observations. The warped structure results in shadows projected on the outer disk where the stellar heating is blocked by the inner disk at PAs of 0.5h and 6.5h. The similarity with the observations (Fig. 8) is remarkable considering the idealizations of the synthetic disk, which assumes a circular cavity, power-laws for the grain size distributions, and steady-state dust trapping prescriptions. Another idealisation of the model is steady state passive heating.

The cooling timescale is $\tau_C = U/(\sigma_B T^4)$, where $U$ is the internal energy per unit area, and $\sigma_B$ is the Stefan-Boltzmann costant. The condition that $\tau_c$ must be shorter than the crossing time under shadows that cover ~20°at 140 AU (Marino et al. 2015, and Fig. 11), is satisfied for surface densities lower than 50 g cm$^{-2}$, which is indeed the maximum surface density in the model. It is thus reasonable to expect that the double-peaked structure of the continuum emission is determined by the temperature field, and that the mm-grains are otherwise uniformly spread along the crescent. The modulation in temperature along the crescent, caused by the inner warp, impacts on the thermodynamics of the disk. This modulation imparts a periodic forcing to the outer disk, whose dynamical consequences should be investigated, and that could perhaps explain the observed spiral pattern.
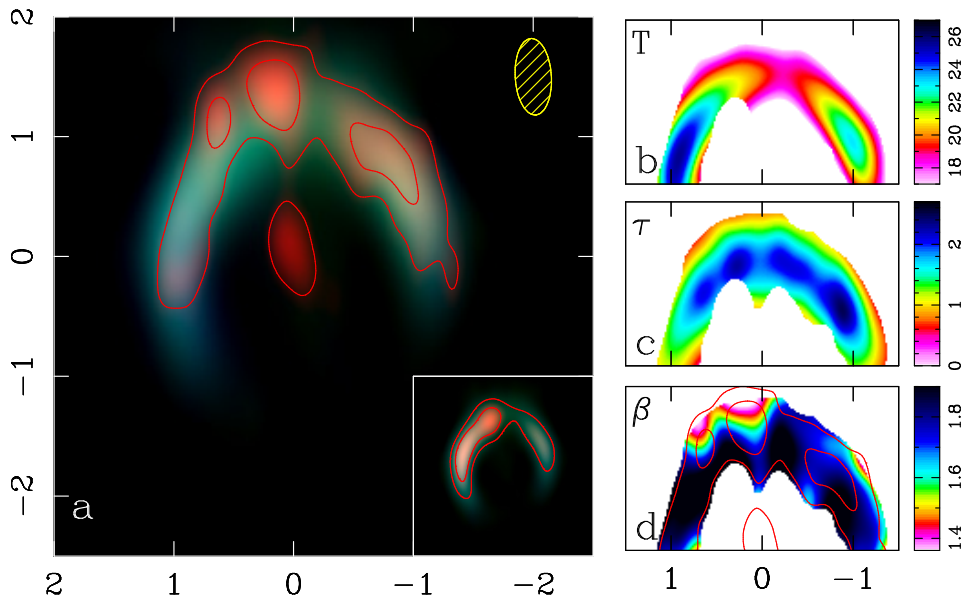
**Figure 2.** Multi-frequency continuum highlighting larger grains at 11.5h. The data have been filtered for the ATCA response. **a**: RGB image with the ATCA image in red (with corresponding contours at 0.4 and 0.7 times the peak intensity at $147\mu$Jy beam$^{-1}$), ALMA band 7 in green, and ALMA band 9 in blue (see Fig. 6 for a panel with the same shown images separately). The inset shows emergent intensities predicted from the dust trap model, after filtering for the ATCA response, with 34 GHz in red contours at 0.5 and 0.75 times the peak. The side of the inset corresponds to 3.5 arcsec. **b**: Observed grey-body temperature map. **c**: optical depths at 345 GHz. **d**: emissivity index map $\beta_s(\vec{x})$, with ATCA contours in red. The $\beta_s$ minimum at 11.5h indicates the presence of larger grains.

### 4.3. *Very lopsided disks?*

The spectral trends in HD 142527 at ALMA frequencies can thus be accounted for with optical depth effects, such that no trapping is required for grains up to 1 mm in size. In other words, the large sub-mm crescent (Casassus et al. 2013) mostly reflects the gas background, with relatively inefficient trapping, so that the observed contrast ratio of $\sim$30 is accounted for with a contrast of 20 in the gas. Marked gaseous asymmetries with contrasts of order 10 are seen in MHD simulations of dynamical clearing by planet formation (Zhu & Stone 2014), and could perhaps reach higher values in models incorporating dead-zones with discontinuous turbulence prescriptions (Regály et al. 2012), or with enhanced cooling inside the dust trap via dust-gas coupling. Thus we propose that other sub-mm asymmetries could partly reflect the gas, perhaps even with contrasts of order $\sim$100 such as in IRS 48, and most likely in the more moderate contrasts, such as in HD 135344B and SR 21 (Pérez et al. 2014).

### 5. CONCLUSION

In summary, the multi-frequency observations of HD 142527 are consistent with the dust trap scenario. New ALMA observations have shown that the mm-grains are so abundant in the crescent that efforts to observe grain growth at sub-mm wavelength are thwarted by optical thickness. Optical depth effects account for the spectral trends at ALMA frequencies, while shadowing of UV-optical radiation by the central warp explains the temperature structure of the crescent. However, at transparent cm-wavelengths a compact clump of approximately cm-sized grains is embedded within the broader crescent of smaller mm-grains (the exact grain sizes depends on the size distributions). These phenomena are expected in the context of the aerodynamic coupling of dust grains with pressure gradients, given the physical conditions in the passively heated outer disk of HD 142527. Prospects are good for witnessing planetesimal formation by dust trapping with radio observations of HD 142527 at cm-wavelength.

## APPENDIX

### A. OBSERVATIONS

HD 142527, at $\sim$140 pc, is a promising laboratory to observe on-going gas giant planet formation, and con-

firm the existence of the dust trap phenomenon. This transition disk has a close to face-on orientation. Infrared observations found an inner disk, ~10 AU (Fujiwara et al. 2006) in radius, and surrounded by a particularly large gap (Fukagawa et al. 2006). A disrupted outer disk (Casassus et al. 2012) beyond 140 AU is indicative of dynamical clearing of the gap by giant planet formation. The cavity is devoid of bodies larger than ~4 $M_{jup}$ (Casassus et al. 2013), but an accreting companion has been reported at ~10 AU (Biller et al. 2012; Close et al. 2014; Rodigas et al. 2014) (with a binary mass ratio of 0.01 to 0.1). The bulk of the mass lies in the outer disk, whose crescent morphology (Ohashi 2008; Casassus et al. 2013) approximately anti-correlates with molecular-line emission (Casassus et al. 2013; van der Plas et al. 2014; Perez et al. 2015). A complex array of trailing spiral arms sprouts away from the outer disk (Fukagawa et al. 2006; Casassus et al. 2012; Rameau et al. 2012; Canovas et al. 2013; Avenhaus et al. 2014; Christiaens et al. 2014).

In this Section we provide details on the datasets that sustain our multi-frequency analysis. Sec. A.1 presents the new ALMA observations, Sec. A.2 presents the new ATCA data and Sec. A.3 summarizes previously published ALMA data. Sec. A.4 briefly describes our image synthesis procedure, while Sec. A.5 and Sec. A.6 describe the alignment of the multi-frequency ALMA data and associated spectral index trends and Sec. A.7 describes the alignment of the ATCA and ALMA datasets.

### A.1. *ALMA band 9 observations*

ALMA Band 9 observations of HD 142527 for program JAO.ALMA#2011.0.00465.S were carried out in 2012, in the nights of June 3, from 02:52:53 to 04:39:10 UT, and on June 4, from 00:43:22 to 02:42:26 UT. The precipitable water vapor (PWV) in the atmosphere was stable between 0.54 mm and 0.62 mm on June 3, with a median value at zenith of 0.581 mm. Conditions on June 4 were similar, with a median PWV at zenith of 0.597 mm. The ALMA correlator provided 1875 MHz bandwidth in four different spectral windows at 488.28125 kHz resolution (or 211.67 m s$^{-1}$ at 691.47308 GHz) per channel. Each spectral window was positioned in order to target the CO(6-5) transition at 691.47308 GHz, HCO$^+$(8-7), H$^{13}$CO$^+$(8-7), and HCN(8-7). Only CO(6-5) was detected. This line is the topic of a separate article. On June 3, the measured system temperatures ranged from ~ 1400 ± 500 K in the spectral window covering CO(6-5) to ~ 2000 ± 700 K in the spectral window covering HCO$^+$. System temperature values 100 to 200 K higher were recorded on June 4. The number of 12 m antennas available at the time of the observation was 20, although one antenna reported very large system temperatures (DV12), and was flagged during data reduction. Excluding calibration overheads, the total time on source for HD 142527 was 43 min on June 3, and 49 min on June 4. The primary flux calibrator was Titan, while 3C279 was used as bandpass calibrator. We used J1517-243 as phase calibrator, for which we measure a flux density of 0.70±0.14 Jy at 702 GHz, where the uncertainty accounts for systematic calibration errors. This measurement is consistent with historical values for this source. The radiometer phase correction errors were large enough to decorrelate the signal. We used the self-calibration algorithm to determine improved antenna-

based phases that were consistent with the continuum image of HD 142527.

### A.2. *ATCA data*

We used ATCA to observe HD 142527 in several array configurations in May 2010 (6A), June 2010 (6C), July 2013 (6A) and August 2013 (H168), with maximum baselines extending to 6 km. The Compact Array Broadband Backend, or CABB (Wilson et al. 2011), provides two sidebands with bandwidths of 2 GHz in 2024 channels each. We centred each sidebands at 19/21, 23/25, 33/35 and 41/43 GHz (in this work we focus on the 33/35 dataset). Complex gains were derived from observations of the quasar 1600-44, separated by about 2.8 degrees on the sky from HD 142527. The gain calibrator was typically observed every 5 to 15 min for between 1 and 3 min duration, dependent on atmospheric conditions. Pointing checks were also made on the quasar every 60-90 min. The bandpass response was determined from 15 minute observations of the quasar 1253-055 (3C 279). The absolute flux calibration was performed using ATCA's primary cm-band flux calibrator, the quasar 1934-638. All subsequent data reduction and calibration was performed with the Miriad software (Sault et al. 1995). The CABB setup at 33/35GHz was used in 4 runs with different array configurations, including H168, which allows us to estimate that the amount of flux loss in the extended configurations is negligible. The flux densities obtained in H168, 1.28±0.04/1.48±0.04, in Jy, for each sideband centered at 33/35GHz, is indistinguishable from the values of 1.23±0.05/1.49±0.06, 1.34±0.11/1.48±0.11 and 1.25±0.13/1.24±0.09 obtained in 6C, 6C and 6A, respectively.

The ATCA data with the best dynamic range was obtained in Ka, i.e. at 33 GHz / 35 GHz. For efficiency we averaged each CABB 2 GHz spectral window into 8 channels. We then brought all of the 6 km visibility data in Ka to a common epoch, which we chose as July 2012, by correcting for the source proper motion with a translation phase (using the Miriad task `uvedit`). The 6 km data in Ka were then concatenated with the task `concat` from `CASA` (McMullin et al. 2007) version 4.2.2. A standard clean restoration revealed a faint modulation at low spatial frequencies in the field, atypical of image synthesis artifacts and reminiscent of phase calibration errors. We therefore applied selfcalibration of the visibility phases, using the `clean` model and the `CASA` tasks `gaincal` and `applycal`. We used a solution interval of 30 min and combined both spectral windows for sensitivity. The `clean` restoration of the corrected visibilities results in essentially the same source morphology as the uncorrected dataset, but with less systematics in the field. The impact of self-calibration can be assessed by inspection of Fig. 3, where we show the restored images obtained with our `uvmem` (Casassus et al. 2006, 2013) tool before and after self-calibration (more information on this image synthesis is given in Sec. A.4 below).

### A.3. *Previous ALMA band 7 observations*

As explained in Fig. 4 and Sec. A.5, the calibrated dataset ALMA#2011.0.00465.S is affected by faint outliers. We therefore used the ALMA Band 7 obtained by Fukagawa et al. (Fukagawa et al. 2013),
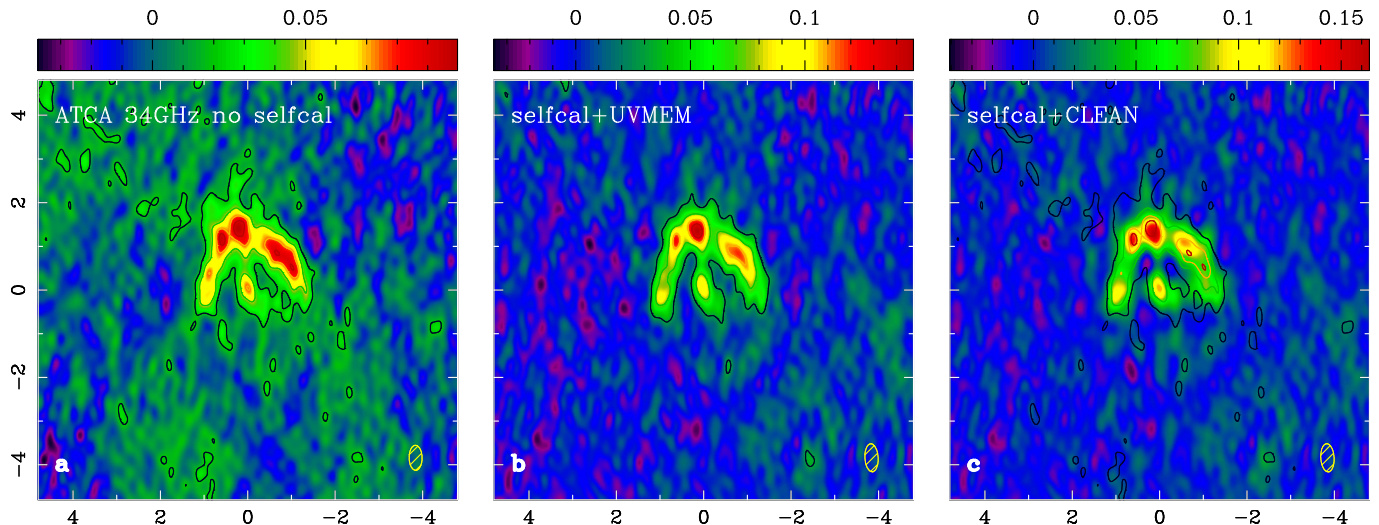
**Figure 3.** Comparison of the restored ATCA images and the impact of self-calibration. The wedges indicate specific intensity in mJy beam$^{-1}$. **a)** no self-calibration ( `uvmem` restoration with a beam of $0.570 \times 0.296$ arcsec$^2$). **b)** self-calibrated image with `uvmem` restoration (with a beam of $0.639 \times 0.302$ arcsec$^2$). **c)** self-calibrated image with `CASA` (McMullin et al. 2007) `clean` restoration (with a beam of $0.644 \times 0.304$ arcsec$^2$, `CASA` version 4.2.2).

ALMA#2011.0.00318.S, keeping only the last scheduling block, observed on 10-Aug-2012. The reason for not combining the whole dataset is because the dynamic range under the crescent is limited by image synthesis, rather than thermal noise, and because pointing uncertainties would degrade the beam if combined without a tedious alignment procedure (see Sec. A.5). For instance, we measured an offset of 0.065 arcsec between this scheduling block and the single scheduling block in band 7 from ALMA#2011.0.00465.S, comparing exclusively the common spectral window at 342.8 GHz. These offsets are within the nominal pointing accuracy of ∼0.1 arcsec. Although small, such offsets have appreciable consequences when deriving spectral index maps.

In summary, we used the dataset acquired by Fukagawa et al. (Fukagawa et al. 2013), program JAO.ALMA#2011.0.00318.S but tied the astrometric pointing to the data previously presented by Casassus et al. (Casassus et al. 2013), JAO.ALMA#2011.0.00465.S. Further details on the astrometric registrations are given in Sec. A.5 and A.7.

### A.4. Image synthesis

For image synthesis we use a non-parametric least-squares modeling technique (Casassus et al. 2006) with a regularizing entropy term (i.e. as in the family of maximum entropy methods, MEM). We call this tool `uvmem`. These deconvolved model images are 'restored' by convolution with the clean beam and by adding the dirty map of the visibility residuals calculated using the `CASA` package, for a chosen weighting scheme. In this work we used natural weights.

The `clean` algorithm is an efficient and widely accepted technique to produce images from radio-interferometer data. To produce consensus images that can be compared with our own `uvmem` tools we used standard `CASA` clean, i.e. Cotton-Schwabb. A comparison between `uvmem` and `clean` is shown in Fig. 3.

We assume that the relative values of the visibility weights in the ALMA data are accurate. However, the absolute values do not match the scatter in the visibility samples recorded at each integration. In order to extract statistics and perform least squares fits, we therefore scaled the weights so that they correspond to $1/\sigma^2$, where $\sigma$ is the root mean square dispersion of all the visibility samples recorded for a given baseline and channel. This procedure was carried out using a tool we call `uvreweight`. A single scale factor was applied to the weights of the whole dataset, given by the median values of the ratios between observed scatter and tabulated weights. Thus we respected the relative values of the weights as provided in the calibrated dataset. We used median averages for a robust estimate of the observed scatters, after correction by the median absolute deviation. In this `uvreweight`-processed data the absolute value of the weights can be used to extract statistics.

### A.5. Alignment of the multi-frequency ALMA data

We aligned the multi-frequency interferometer data by cross-correlating the visibilities, as illustrated in Fig. 4. We first approximately bring two independent visibility datasets to a common $uv$-coverage in the following way. We select as reference the dataset with the more compact $uv$-coverage (usually the lower frequency), and produce a deconvolved model using `uvmem` of the visibility dataset with the more extended $uv-$coverage. We then compute synthetic interferometer data corresponding to the more compact $uv-$coverage using our tool `uvsim`. For consistency the procedure is also applied to the reference. Having produced comparable visibility datasets, we regularly sample shifts in the world coordinate systems (WCS) of the two frequencies in a uniform grid of positional offsets $\{\vec{\delta_i}\}$ (assuming that the parallactic calibration is perfect in both cases).For each WCS offset $\vec{\delta_i}$ we computed shifted band 9 visibilities

$$V_{b9}^{\text{shift}}(\vec{u}_k) = V_{b9}(\vec{u}_k) \exp\left[i 2\pi (\vec{\delta_i} \cdot \vec{u}_k)\right].$$
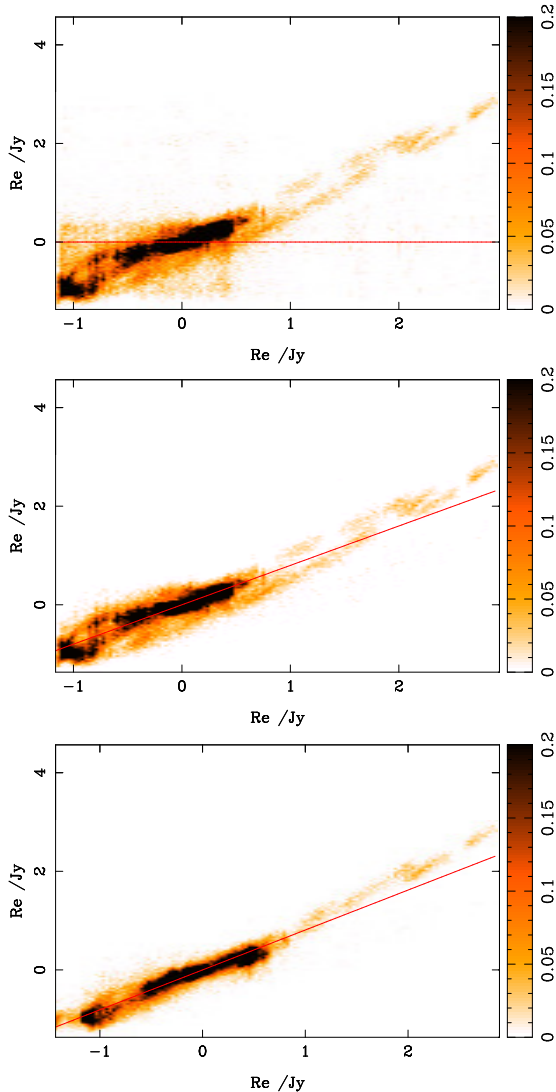
**Figure 4.** Band 7 vs. Band 9 visibility scatter plot, from dataset `2011.0.00465.S`. Top: cross-correlation before outlier filtering. Middle: after outlier filtering, but before astrometric WCS correction. Lower plot: after the alignment procedure described in Sec. A.5. In this case, the applied WCS offset is (-0.063″, -0.016″) along R.A. and Dec. We see here that this band 7 dataset ALMA#2011.0.00465.S is affected by faint outliers, this is why we used the data from ALMA#2011.0.00318.S (Fukagawa et al. 2013). Since the dynamic range under the crescent is not limited by thermal noise, we kept only the last scheduling block, observed on 10-Aug-2012, to minimize pointing offsets. For consistency we tied the astrometric pointing to `2011.0.00465.S`.

We then calculated a linear regression between real and imaginary parts of visibilities, used as independent data, and computed the $L_2$ distance (squared norm) between model and data. We form an image $\chi^2(\{\vec{\delta_i}\})$ of the $L_2$ distances for each $\vec{\delta_i}$. The best WCS shift is given by the centroid $\vec{\delta_o}$ of an elliptical fit to $\chi^2(\{\vec{\delta_i}\})$. Although we measure the shifts $\vec{\delta_o}$ in the $uv-$plane, the actual application of $\vec{\delta_o}$ to bring images to a common WCS system is carried out after image restoration, so in the image plane.

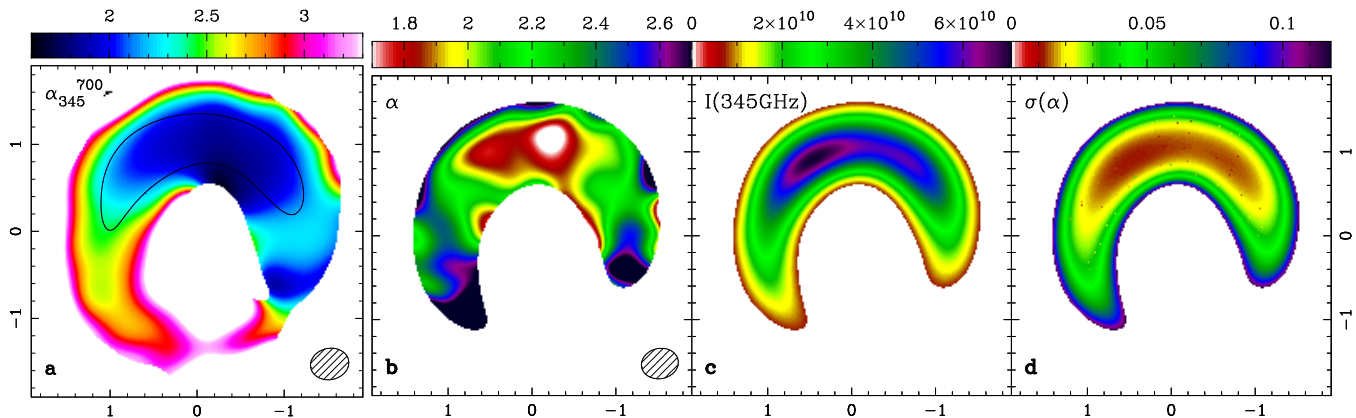### A.6. Spectral index maps

Thanks to the positional alignment procedure, we can build a Band 7/Band 9 spectral index map by bringing both datasets to an approximately common $uv$-coverage, as outlined in Sec. A.5. We then compute restored images of the `uvmem` models. The resulting Band 7/Band 9 spectral index map is shown in Fig. 5. We caution that the absolute values of the spectral index map $\alpha$ is dependent on the chosen absolute flux calibration and SED, as explained in Sec. D. However, the relative variations in $\alpha$ are significant, and independent of the chosen scale. Fig. 5 corresponds to the flux scale labelled *C13scale* (see Sec. D).

In order to build a spectral index map based on the intra-band frequency lever of the ALMA band 7 data, we selected the lowest frequency spectral window as reference $uv$-coverage. For instance in the spectral fits to the intra-band spectral windows (SPWs) of the ALMA band 7 data ALMA#2011.0.00318.S, this corresponds to 329.3 GHz. We then bring all 4 spectral windows in band 7 to a comparable $uv$-coverage, by following the procedure outlined in Sec. A.5 (so the reference SPW was also processed in the same way as the other 3 SPWs).

Once all four spectral windows are brought to a comparable $uv-$coverage, we extract a spectral index map by fitting the restored specific intensity maps with a power-law. There are therefore two free parameters per pixel, the intensity at the reference frequency, and the power-law exponent. Fig. 5 shows the resulting fit, along with the 1 $\sigma$ error on the spectral index. We caution that the absolute values of this intra-band spectral index map depends on the choice of SED scale, as explained in Sec. D. However, the morphological trends are independent of the total flux density scale.

### A.7. Alignment of the ATCA and ALMA data

The offset between the ATCA and the ALMA Band 7 data from ALMA#2011.0.00465.S was within our measurement errors. Since in the ATCA data we have two IFs centered on 33 GHz and 35 GHz, we can test the alignment by cross-correlating each IF separately, as in Sec. A.5, and also by requiring consistency between real and imaginary parts. It turned out that the ATCA/Band 7 offset is systematically smaller than 0.15″, and changes sign. We concluded that the ATCA and ALMA pointing are consistent, but that the morphologies are too different for a more refined alignment with our cross-correlation scheme. We also attempted the standard strategy of identifying a common anchor point, in this case the stellar position. We document this exercise as it bears on the morphology of the signal from the star's vicinity in ALMA band 7. The central free-free signal, at the limit of dynamic range in band 7, is difficult to use as astrometric reference as its morphology is sensitive to self-calibration, and varies from a compact inner disk reported by Fukagawa et al. (2013) to a gap-crossing filament in our previous analysis (Casassus et al. 2013). However, the continuum filament we image in our self-calibrated band 7 data, after filtering for outliers using our tool `uvreweight`, culminates in a local maximum near the central star, now in closer agreement with Fukagawa et al. (2013). Given the uncertainties affecting the very faint stellar signal in

**Figure 5.** Spectral index map from the aligned images of the ALMA Band 7 and Band 9 datasets. **a)** spectral index from the comparison between band 7 and band 9, $\alpha_{345}^{700}$. The single contour shows the Band 7 continuum traced at half-maximum. **b-d)** Power-law fits to the intra-band 7 ALMA data, using dataset ALMA#2011.0.00318.S (Fukagawa et al. 2013). **b)** spectral index map $\alpha(\vec{x})$. **c)** best-fit amplitude at the reference frequency of 345 GHz, in Jy/sr. **d)** thermal uncertainty on the spectral index map.

band 7, the default astrometries for ATCA and ALMA band 7 ALMA#2011.0.00465.S appear to be consistent. We note, however, that the 11.5h emission appears to extend outwards in radius, by about $0.3 \pm 0.1''$ compared to ALMA band 7, while the 1h clump does not. But given the above pointing uncertainties, this effect is not significant enough to warrant further consideration and modeling. We brought the multi-frequency data of HD 142527 to a common $uv-$coverage following the same procedure as for the multi-frequency ALMA data. The main difference is that here we used the ATCA data as reference. The resulting restored images are shown in Fig. 2a, where the origin of coordinates corresponds to the location of HD 142527 at the Jun 2012 epoch. The central point source at 34 GHz is satisfactorily aligned with the origin.

## B. MONTE-CARLO TESTS FOR THE MULTI-FREQUENCY MORPHOLOGICAL DIFFERENCES

Images obtained with pre-ALMA radio-interferometry are known to be affected by $uv$-coverage artifacts, especially with ATCA. Despite the efforts invested in covering the $uv$-plane in several ATCA runs, with different array configurations, it is important to test for such $uv$-coverage artifacts, that could for instance inject the 11.5h local maximum. We first produce deconvolved model images of the ALMA band 7 and band 9 visibility data using our tool `uvmem`, and then simulate ATCA observations on these model images, following exactly the same $uv$-coverage as in the ATCA 34GHz concatenated data using our tool `uvsim`. The simulated visibilities are then scaled by a linear regression (forced to cross the origin), so that the simulated and ATCA visibilities are comparable in magnitude. Following this scaling, we inject thermal noise given by the observed visibilities weights (having first applied our tool `uvreweight` to replace the ATCA visibility weights by the observed scatter). We repeat this procedure 200 times before taking statistics. Fig. 6 summarizes the result of these Monte-Carlo simulations. We see that the signal is more extended in the

ALMA bands than it is in ATCA, so that the visibility scaling we applied results in lower signal-to-noise ratio than in the actual ATCA observations. In this sense our MC simulations are conservative, we are injecting more noise relative to the signal (by about 40% in band 7). The final rms dispersions are up to $\sim 1/7$ of the differences between the ATCA and ALMA images - in other words, the differences between ATCA the ALMA images range from $-3\sigma$ to $+6.2\sigma$. The reduced $\chi^2$ taken over pixels where both ATCA and ALMA are above 1/3 of the peak, is 4.2 for band 7, and 4.9 for band 9, for 12 independent data points (the number of ATCA beams enclosed in the 0.3 times maximum contour) - the images are thus different with a very high confidence level. In particular, under the 11.5h clump (so at the ATCA maximum), the difference with the band 7 average is 5.9 times the band 7 rms.

An additional test was performed by subtracting the synthetic band 7 ATCA visibilities from the 34 GHz ATCA data, after appropriate scaling by linear regression. The stellar emission stands out in the residuals, as well as the 11h ATCA clump. These significant residuals, both positive and negative, point to genuine morphological differences between 34 GHz and 345 GHz. In particular, the peak residual corresponding to the 11h clump is at 50 $\mu$Jy beam$^{-1}$, while the thermal noise is at 10 $\mu$Jy beam$^{-1}$.

## C. COINCIDENCE BETWEEN ATCA MAXIMA AND MOLECULAR LINE DECREMENTS

The 34 GHz clumps coincide with the molecular-line decrements in HCO$^+(4-3)$ and in CO$(3-2)$ that have been previously documented (Casassus et al. 2013). It has been suggested that an optically thick continuum may somehow be responsible for the correlation of the $^{12}$CO decrements with the 345 GHz crescent (Casassus et al. 2013; van der Plas et al. 2014). Indeed, as shown in Fig. 7, the synthetic dust trap model documented below readily reproduce such decrements with a dust to gas mass ratio of 94, a standard CO abundance of $10^{-4}$, and
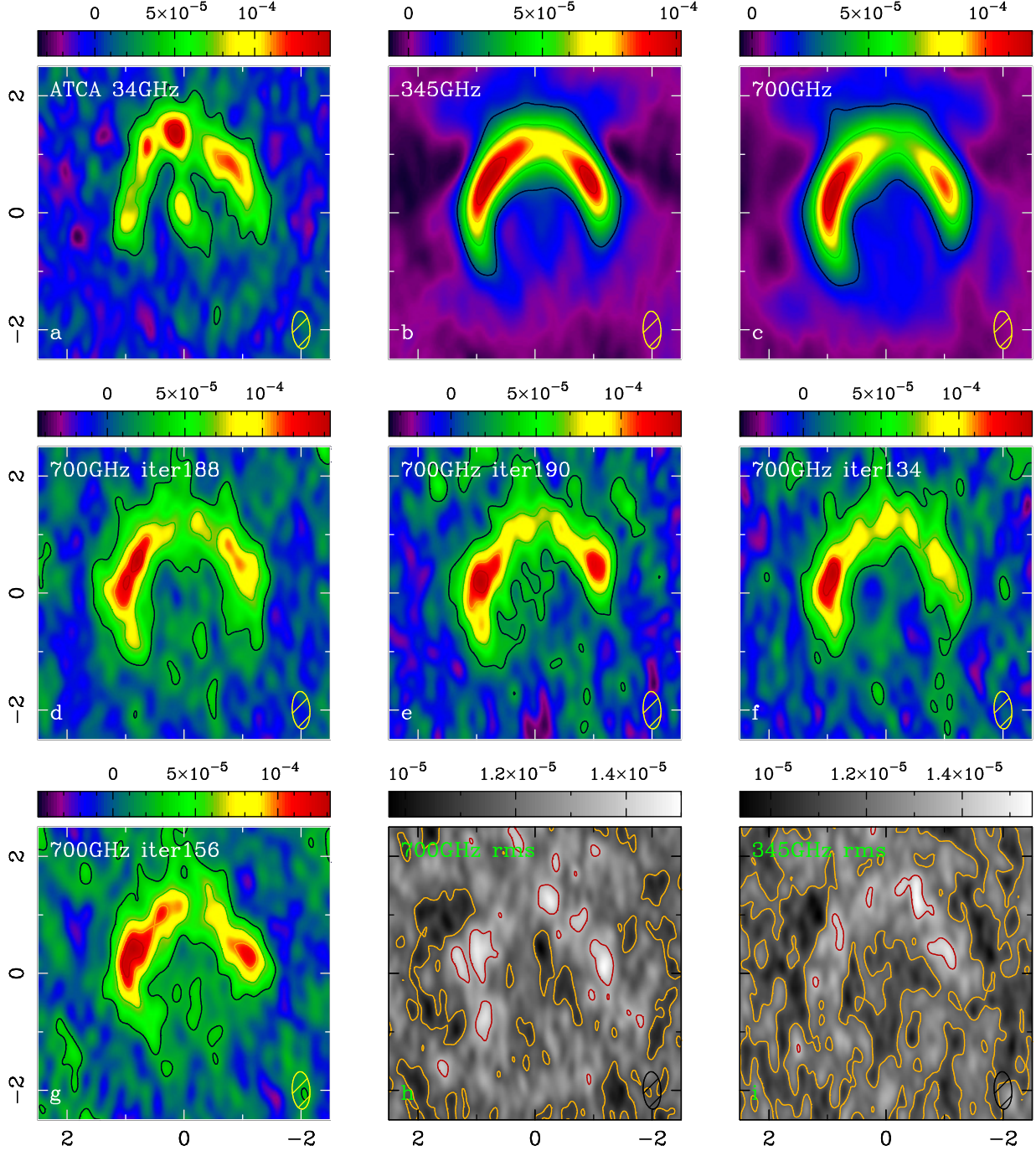
**Figure 6.** Statistics of the multi-frequency morphological differences inferred from Monte-Carlo (MC) simulations. All images have been restored from `uvmem` models. **a)**: restored ATCA image at 34 GHz. **b)**: average of ATCA observations with 200 realizations of noise on the band 7 data. **c)**: average of the MC simulations for band 9 **d)-g)**: different realizations of noise. **h)**: rms scatter of the band 9 simulations. **i)**: rms scatter of the band 7 simulations.

the following temperature profile:

$$T = 70 \text{ K, if r} < 30 \text{ AU, or} \quad \text{(C1)}$$
$$T = 70 \text{ K(r/(30 AU)}^{-0.5} \text{ if r} \geq 30 \text{ AU.}$$

However, setting the gas temperature to a representative dust species in the outer disk (we chose the average population of amorphous carbon grains) attenuates the depth of the decrements - they are restricted to the outline of

the underlying optical depth field. The decrements are reproduced by the above prescription for the gas temperature because the gas temperatures in the crescent, at $r = 140$ au, are $\sim$30 K, and cooler than the continuum temperatures in the model, which reach 50 to 60 K. Thus in this case the gas acts like a cold foreground on a hotter continuum background, which after continuum subtraction appears like foreground absorption. In fact, CO at higher altitudes could be hotter than the background
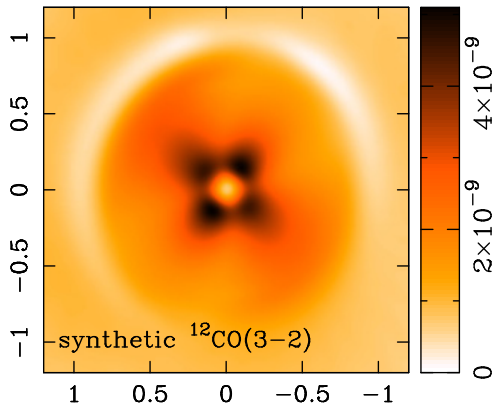
**Figure 7.** Frequency-integrated image of the $^{12}$CO(3-2) emission calculated with RADMC3D on our preferred model for the dust trap of HD 142527. $x-$ and $y-$ axis indicate offset from the stellar position along R.A. and Dec., in arcsec.

continuum, so could still stand out after the subtraction of a colder optically thick continuum. Yet the gas temperature prescription above is inspired by the molecular line data, and higher temperatures can be ruled out as they greatly overestimate the integrated CO line fluxes.

### D. ABSOLUTE FLUX SCALE

The inferred grey-body diagnostics and spectral index maps depend on the absolute calibration of the input multi-wavelength data. There are however substantial uncertainties on the observed SED. For instance, the flux densities reported for different ALMA programs in band 7 vary by up to 50%, (Casassus et al. 2013; Fukagawa et al. 2013). The band 9 flux densities are affected by similarly large uncertainties. The *Herschel* SPIRE flux density (van der Wiel et al. 2014) at the same frequency is 13.7 Jy. We investigated two plausible scenarios for the observed SED. The pectral trends reported here are derived from the first of these flux scales, which we label *C13scale*, where we adopted a reference band 7 flux density of 3.5 Jy at 345 GHz, and took the SPIRE flux density for band 9. The comparison between the SPIRE flux density and the band 7 levels implies a spectral index $\alpha_{b7}^{b9} \sim 1.9$. On the other hand, the band 6 ALMA data at 250 GHz (Perez et al. 2015) yields $\alpha_{b6}^{b7} \sim 2.7$. We thus assumed that a plausible value for the intra-band 7 spectral index is $\alpha_{b7} = 2.2$.

The synthetic dust trap, documented below, fits the SED within the error bars. So, for the purpose of comparing the observations with the synthetic dust trap predictions, we also considered a second flux sale, which we labelled *SEDscale*. This scale has a rather high band 9 flux density of 15.7 Jy at 700 GHz, and is rather low in band 7, with 2.17 Jy at 342.9 GHz, while it comes very close to the reported flux density at 34 GHz, with 1.34 mJy. All morphological trends are similar in both flux scales, but the highest optical depths in the *SEDscale* are lower - dropping by about 2.5 in *C13scale* to 0.7 in *SEDscale* (at 345 GHz). The temperature map appears to be more irregular in *SEDscale*, which suggests that *C13scale* may be more realistic.

### E. LINE OF SIGHT TEMPERATURES AND OPTICAL DEPTHS

The grey-body uniform-slab models are used as diagnostics for the optical depth, and are meant to characterize the emergent spectrum at a given line of sight with three parameters, adjusted to three frequency points. By applying the grey-body diagnostic to the ALMA band 7 amplitude and slope, and including band 9, we find that the crescent is optically thick in band 7. Fig. 8 shows that grey-body line-of-sight models provide a fit to the observations, despite the use of a constant emissivity law $\beta_S(\vec{x}) = 1.5$. We used the *C13scale* flux-density scale; *SEDscale* produces similar maps but the low band 7 flux density results in lower optical depths. We also applied the grey-body diagnostic to the ATCA/ALMA multifrequency data, as summarised in Fig. 9. The temperature map is essentially fixed by the band 9 spectral point. We note a minimum in temperature towards 0.5 h, which is also seen when using the ALMA data alone. The similarities between both temperature maps in *C13scale* is surprisingly good, considering the differences in *uv*-coverage, and the different treatments for $\beta$.

The uncertainties on the opacity index $\beta_S(\vec{x})$ were estimated by varying the ATCA intensities by $\pm 1\sigma$, where $\sigma$ is the scatter in the dirty map of image synthesis residuals. The resulting uncertainty map is shown in Fig. 9. The peak at 34 GHz, under the 11.5h clump, corresponds to $\beta_S = 1.18 \pm 0.04$ (in the *SEDscale*, similar significance values are obtained in the *C13scale*), whereas the average value outside the regions of low $\beta_S$ is 1.50, with a rms dispersion of 0.07 and typical values varying from $1.41 \pm 0.05$ at 1h, up to $1.63 \pm 0.08$ at 9.5h. Compared to the average value of 1.50, the minimum in $\beta_s$ under the 11.5h clump is significant at $\sim 7\sigma$.

### F. SYNTHETIC DUST TRAP MODEL

We constructed a synthetic model of a protoplanetary disk with a dust trap to make predictions comparable to the ALMA and ATCA observations of HD 142527. This synthetic model matches the observed SED (see below), and is a perfected version of that which accounts for the scattered-light shadows (Marino et al. 2015), with a tilted inner disk. This model allows us to 1- assess if the observations can be interpreted with steady-state dust trapping formulae, given the tilted-inner disk, and 2- estimate the biases involved in the uniform-slab grey-body model.

The outer disk is where the dust trap is observed, so we describe it in more detail. It goes from 115 au to 300 au with a rounded disk wall between 115 to 140 au, and is composed of $5.0 \times 10^{-5}$ M$_\odot$ in amorphous carbon grains and of $2.6 \times 10^{-3}$ M$_\odot$ in silicate grains mixed with ices (using the Maxwell-Garnett rule). To simulate the dust trap effect on different grain sizes we used the radial trap model from Pinilla et al. (2012) coupled with the prescriptions for azimuthal trapping from Birnstiel et al. (2013). We first define an axisimmetric gas distribution with a rounded disk wall, as previously described in Marino et al. (2015), but with adjusted parameters $\gamma = 7$, $w = 0.13$ and $r_c = 155.0$ au. We compute a critical grain size (Pinilla et al. 2012) $a_c$ at 133 au for which bigger particles would be radially trapped in the pressure maximum, while smaller particles would follow the gas
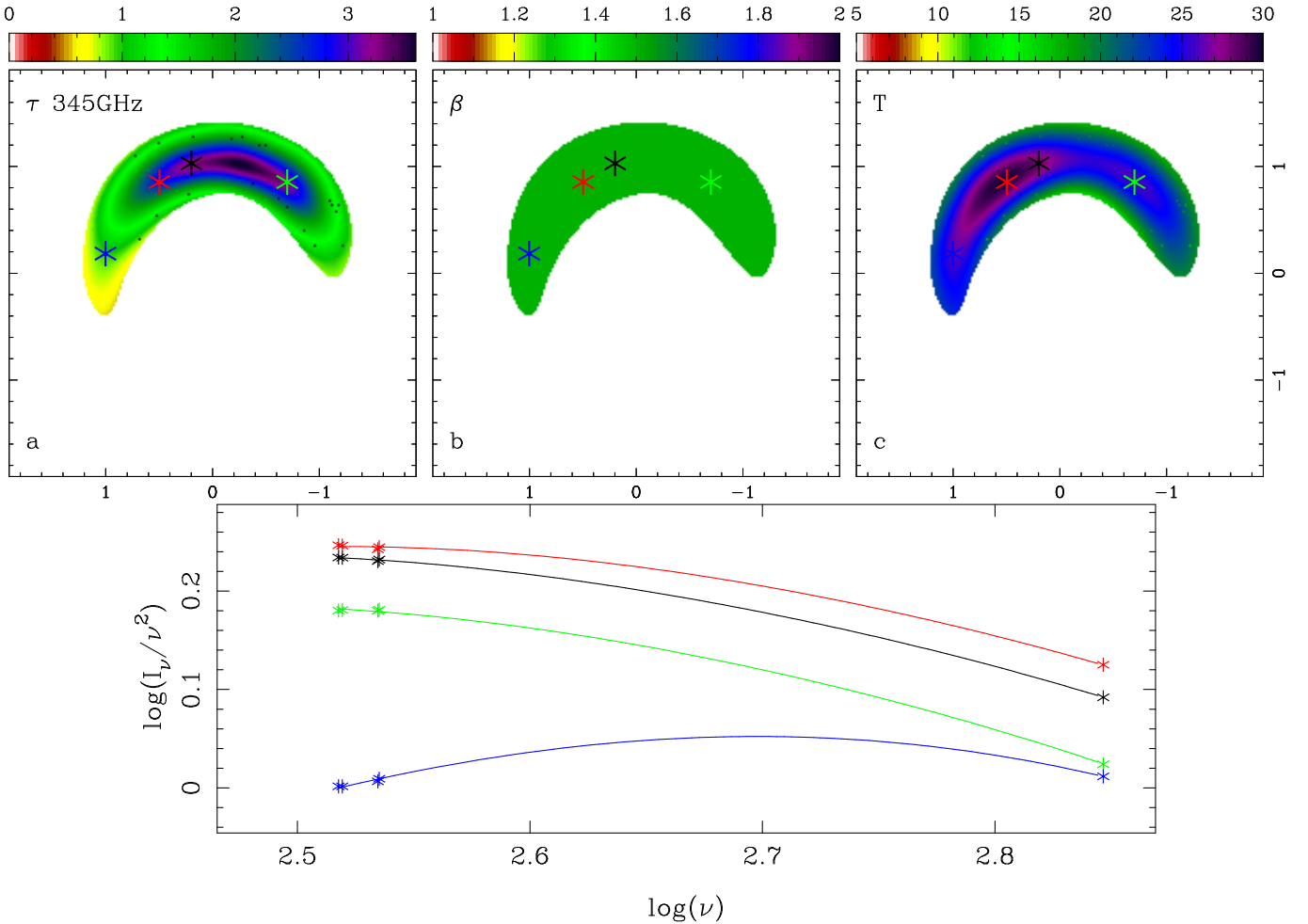
**Figure 8.** Spectral properties of the sub-mm continuum, obtained by comparing the intra-band ALMA band 7 spectral information with ALMA band 9, and with flux-density scale labelled *C13scale*. **Upper panel**: **a** optical depth map at 345 GHz, $\tau_\circ(\vec{x})$ **b**: flat emissivity law, taken here as $\beta = 1.5$ - this plot allows to better locate the asterisks that indicate the locations of the example spectra **c**: temperature map $T_s(\vec{x})$. **Lower panel:** example SEDs extracted at selected positions, indicated by asterisks in the upper panel. The $y$-axis shows specific intensity normalized by a $\nu^2$ spectrum, in arbitrary units.

density background. Using a total gas mass of 0.25 $M_\odot$ and an $\alpha_t$ viscous parameter of $10^{-2}$ we obtain a critical grain size of 0.7 cm at 133 AU. The Stokes number for 0.7 cm grains, at peak gas densities of $2.6\ 10^{10}$ cm$^{-3}$ and 20 K, is $\sim$0.02 and close to $\alpha_t$.

The above radial distribution is modulated in azimuth, using previously described formulae and symbols (Birnstiel et al. 2013) (here we use $R_s = 148$ AU, and an azimuthal contrast in surface density of $c = 20.0$). The scale-height $H$ is given by

$$H(r) = 20.0 \left(\frac{r}{130\ \mathrm{AU}}\right)^{1.17}.  \quad (F1)$$

For the gas volume density we used the standard vertical Gaussian distribution. The small grains, i.e. amorphous carbon and silicate grains smaller than $a_c$, follow the same density field as the gas. The azimuthal distribution of big grains is calculated according to their Stokes number, a parameter to account for the gas turbulence $\alpha_t$ and the gas background (Birnstiel et al. 2013). For their radial distribution we use a Gaussian parameterisation

to account for the spread caused by turbulence:

$$\rho_{d,a}(r,\phi,z=0) = \rho_{d,a}(\phi) \exp\left[-\frac{(r-R_s)^2}{2\sigma^2}\right],  \quad (F2)$$

with $\sigma(a) = H_r \sqrt{\frac{\alpha_t}{St(a)}}$. In order to compute the density as a function of height $z$, we use the same scale height as the gas. We investigated the implementation of grain settling, following a parameterisation for the dust scale height (Armitage 2010). However, we found that in order to reproduce the projection effect at $\sim$1h, settling had to be very inefficient. Finally the distribution of big grains is normalized to the global grain size distribution and total dust mass in big grains.

We used RADMC3D (Dullemond et al. 2015) to transfer the stellar radiation through the synthetic disk and predict emergent intensity maps, under the assumption of passive heating. We assumed a standard power-law distribution in grain sizes, with exponent $-3.5$. The outer disk is composed of three different dust species representing a range in sizes described by $a_{\min}$ and $a_{\max}$:
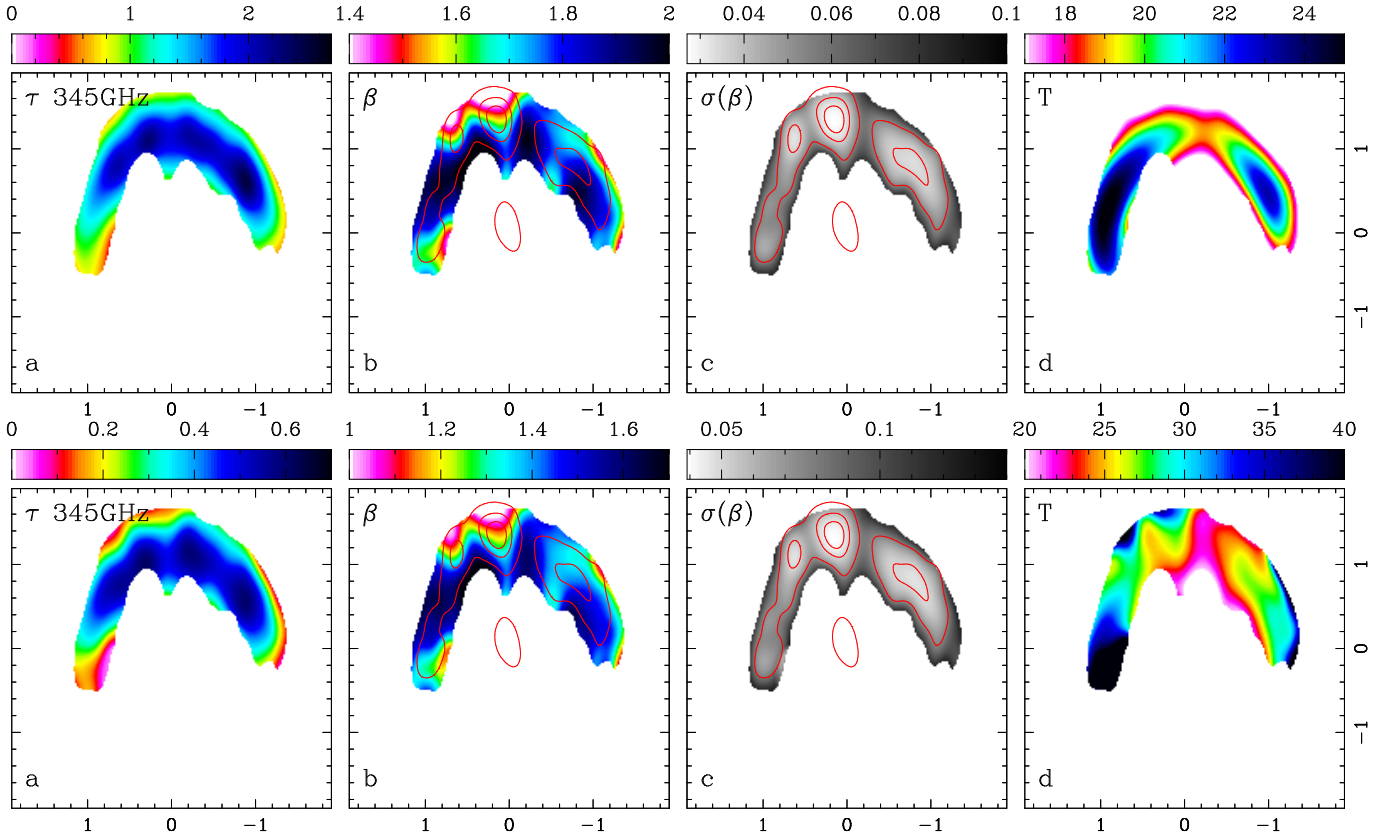
**Figure 9.** Optical depth maps derived from the ATCA/ALMA multi-frequency data. The emissivity minimum at 11.5h indicates the presence of larger grains. The **upper panel** corresponds to the absolute flux density scale labelled *C13scale* in Sec. D, with a high flux density in band 7 (see Sec. D), while the **lower panel** corresponds to the flux scale in our preferred RADMC3D model, labelled *SEDscale* (see Sec. D). **a**: optical depth map at the reference frequency of 345 GHz. **b**: line of sight emissivity index map $\beta_s(\vec{x})$, with ATCA specific intensity contours in red. **c**: root-mean-square uncertainties on the emissivity index map. **d**: line of sight temperature, $T_s(\vec{x})$.

- $5.0 \times 10^{-5}$ $M_\odot$ of amorphous carbon grains with radii $1 < a < 100$ $\mu$m with optical constants taken from Li & Greenberg (1997)

- $2.5 \times 10^{-3}$ $M_\odot$ in icy silicate grains, with radii of $100\mu$m $< a < a_c$ and optical constants from Henning & Mutschke (1997) and Li & Greenberg (1998)

- $1.0 \times 10^{-4}$ $M_\odot$ in icy silicate grains, with radii of $a_c < a < 1$cm and optical constants from Henning & Mutschke (1997) and Li & Greenberg (1998)

As summarised in Fig. 10, the predicted integrated flux densities fall close to the observed dereddened SED, extracted from previous SED fitting experiments (Verhoeff et al. 2011; Perez et al. 2015), and from the *Herschel* archive. Fig. 11 shows that the model also reproduces the H-band scattered light images (this is a perfected version of Fig. 2 in Marino et al. 2015). We switched-off scattering for the purpose of calculating images at sub-mm frequencies and lower. The reason for this is that the scattering cross sections calculated using Mie theory are probably overestimated, given that the actual grains are probably irregular in shape, or even porous, and so far from the Mie spheres. The emergent intensity maps in Fig. 12 show that the 34 GHz emission exhibits a compact clump at the location of the dust trap, and a more

extended crescent that follows the sub-mm morphology. In order to simulate the ATCA response, we sampled the uv-coverage of the actual ATCA observations, but on the radiative transfer predictions, and then averaged 100 `uvmem` reconstructions with different realizations of noise. This exercise produced sky maps that are remarkably similar to the ATCA-filtered observations. We also note that any flux loss is negligible.

## G. UNIFORM-SLAB DIAGNOSTICS ON THE SYNTHETIC DUST TRAP.

We also applied the line-of-sight diagnostic based on grey-body models to the synthetic emergent intensities. As summarised in Fig. 13, the basic features of the grey-body diagnostics approximate those seen in the data. There is a mild extension of the optical depth map into the northern ansa, which could be emphasized with higher optical depths. The center of the dust trap coincides with a minimum in $\beta_S$. With this synthetic dust trap we can also test for biases in the grey-body diagnostics. The input optical depth map,

$$\tau(345 \text{ GHz}) = \int_0^\infty ds \rho_g(s)$$
$$\int da \sum_i n_i(a,s)\kappa_i(a,345\text{GHz}), \text{ (G1)}$$
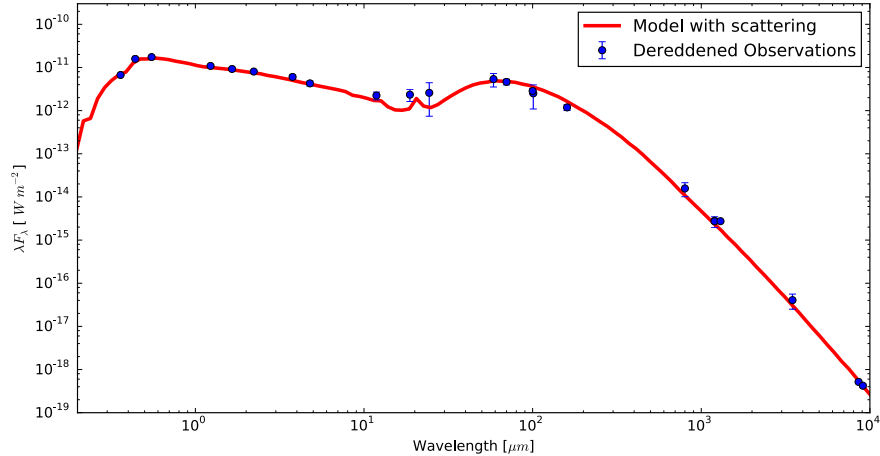
**Figure 10.** Observed and model SED for HD 142527.
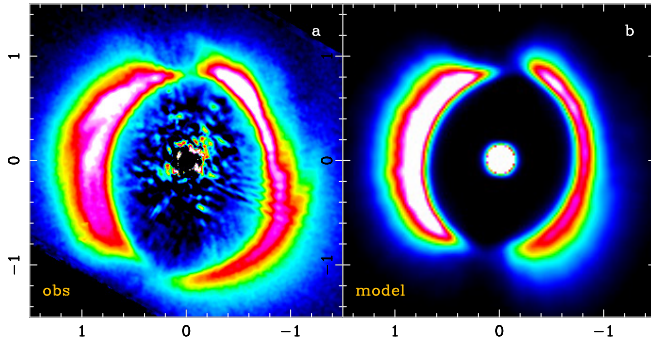


**Figure 11.** Consistency of the synthetic dust trap model with the observed scatterd light shadows. **a:** NACO-PDI H-band image from Avenhaus et al. (2014) **b:** Radiative transfer prediction in H-band from the dust trap model.

is remarkably consistent with the grey-body values - at native resolutions. We can also compare with the grey-body temperature diagnostic, $T_s(\vec{x})$, with the line-of-sight average temperature, as reported by RADMC3D after the thermal solution has converged,

$$\langle T \rangle = \int_0^\infty ds \rho_g(s)$$
$$\int da \sum_i T(a,s)n_i(a,s)\frac{\kappa_i(a,345\text{GHz})}{\tau(345\text{GHz})}. \quad \text{(G2)}$$

Fig. 13 shows that the two temperature diagnostics are very nearly equal (to within 10%). Limiting the integral to the depth $s$ corresponding to $\tau(345\text{ GHz}) = 1$ resulted in essentially identical maps.

*Facilities:* ATCA, ALMA.

<div align="center">REFERENCES</div>

Armitage, P. J. 2010, Astrophysics of Planet Formation (ISBN 978-0-521-88745-8. Cambridge University Press.)
Avenhaus, H., Quanz, S. P., Schmid, H. M., Meyer, M. R., Garufi, A., Wolf, S., & Dominik, C. 2014, ApJ, 781, 87
Ayliffe, B. A., Laibe, G., Price, D. J., & Bate, M. R. 2012, MNRAS, 423, 1450
Biller, B., et al. 2012, ApJ, 753, L38

Birnstiel, T., Dullemond, C. P., & Pinilla, P. 2013, A&A, 550, L8
Bruderer, S., van der Marel, N., van Dishoeck, E. F., & van Kempen, T. A. 2014, A&A, 562, A26
Canovas, H., Ménard, F., Hales, A., Jordán, A., Schreiber, M. R., Casassus, S., Gledhill, T. M., & Pinte, C. 2013, A&A, 556, A123
Casassus, S., Cabrera, G. F., Förster, F., Pearson, T. J., Readhead, A. C. S., & Dickinson, C. 2006, ApJ, 639, 951
Casassus, S., Perez M., S., Jordán, A., Ménard, F., Cuadra, J., Schreiber, M. R., Hales, A. S., & Ercolano, B. 2012, ApJ, 754, L31
Casassus, S., et al. 2013, Nature, 493, 191
Christiaens, V., Casassus, S., Perez, S., van der Plas, G., & Ménard, F. 2014, ApJ, 785, L12
Close, L. M., et al. 2014, ApJ, 781, L30
Dullemond, C., Juhasz, A., Pohl, A., Sereshti, F., Shetty, R., Peters, T., Commercon, B., & Flock, M. 2015, RADMC3D v0.39 http://www.ita.uni-heidelberg.de/dullemond/software/radmc-3d/
Fouchet, L., Gonzalez, J.-F., & Maddison, S. T. 2010, A&A, 518, A16
Fujiwara, H., et al. 2006, ApJ, 644, L133
Fukagawa, M., Tamura, M., Itoh, Y., Kudo, T., Imaeda, Y., Oasa, Y., Hayashi, S. S., & Hayashi, M. 2006, ApJ, 636, L153
Fukagawa, M., et al. 2013, PASJ, 65, L14
Henning, T., & Mutschke, H. 1997, A&A, 327, 743
Kuiper, G. P. 1951, Proceedings of the National Academy of Science, 37, 1
Li, A., & Greenberg, J. M. 1997, A&A, 323, 566
—. 1998, A&A, 331, 291
Lyra, W., Johansen, A., Zsom, A., Klahr, H., & Piskunov, N. 2009, A&A, 497, 869
Lyra, W., & Lin, M.-K. 2013, ApJ, 775, 17
Marino, S., Perez, S., & Casassus, S. 2015, ApJ, 798, L44
McMullin, J. P., Waters, B., Schiebel, D., Young, W., & Golap, K. 2007, ASP Conf. Ser., 376, 127
Mittal, T., & Chiang, E. 2015, ApJ, 798, L25
Ohashi, N. 2008, Ap&SS, 313, 101
Paardekooper, S.-J., & Mellema, G. 2006, A&A, 453, 1129
Pérez, L. M., Isella, A., Carpenter, J. M., & Chandler, C. J. 2014, ApJ, 783, L13
Perez, S., et al. 2015, ApJ, 798, 85
Pinilla, P., Birnstiel, T., Ricci, L., Dullemond, C. P., Uribe, A. L., Testi, L., & Natta, A. 2012, A&A, 538, A114
Pollack, J. B., Hubickyj, O., Bodenheimer, P., Lissauer, J. J., Podolak, M., & Greenzweig, Y. 1996, Icarus, 124, 62
Rameau, J., Chauvin, G., Lagrange, A.-M., Thébault, P., Milli, J., Girard, J. H., & Bonnefoy, M. 2012, A&A, 546, A24
Regály, Z., Juhász, A., Sándor, Z., & Dullemond, C. P. 2012, MNRAS, 419, 1701
Rodigas, T. J., Follette, K. B., Weinberger, A., Close, L., & Hines, D. C. 2014, ApJ, 791, L37
Sándor, Z., Lyra, W., & Dullemond, C. P. 2011, ApJ, 728, L9
Sault, R. J., Teuben, P. J., & Wright, M. C. H. 1995, in Astronomical Society of the Pacific Conference Series, Vol. 77, Astronomical Data Analysis Software and Systems IV, ed. R. A. Shaw, H. E. Payne, & J. J. E. Hayes, 433
van der Marel, N., et al. 2013, Science, 340, 1199
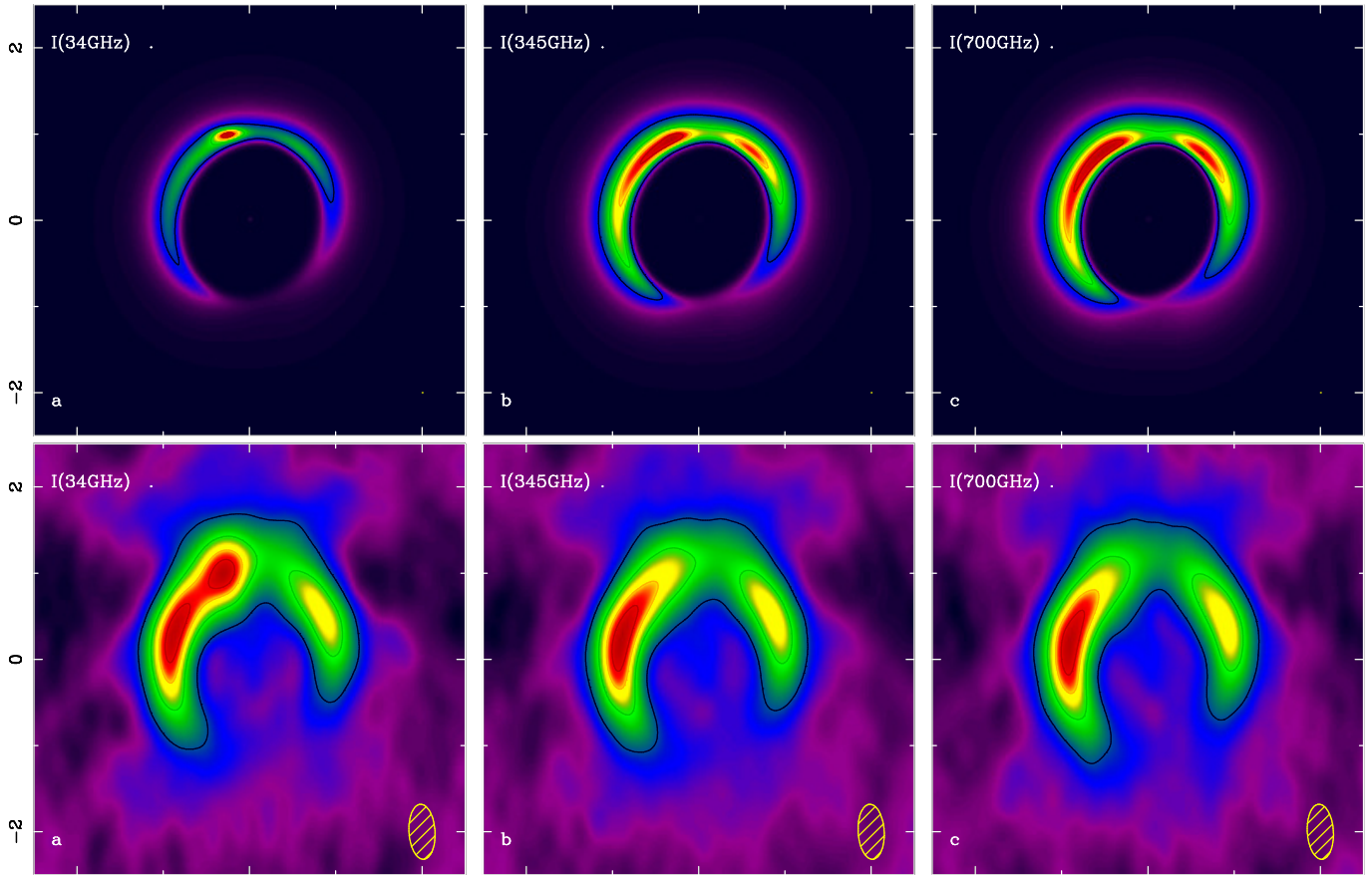
**Figure 12.**    Predicted emergent continua at 34 GHz, 345 GHz and 700 GHz. **Upper panel:** raw RADMC3D prediction. **Bottom panel:** predictions filtered by ATCA+`uvmem` response, with restoration in natural weights. Note the 11.5h clump of cm-sized grains, which stands out at ATCA frequencies, but is absent at ALMA frequencies.

van der Plas, G., Casassus, S., Ménard, F., Perez, S., Thi, W. F., Pinte, C., & Christiaens, V. 2014, ApJ, 792, L25
van der Wiel, M. H. D., et al. 2014, MNRAS, 444, 3911
Verhoeff, A. P., et al. 2011, A&A, 528, A91+
Weidenschilling, S. J. 1977, MNRAS, 180, 57
Wilson, W. E., et al. 2011, MNRAS, 416, 832

Zhu, Z., & Stone, J. M. 2014, ApJ, 795, 53
Zuckerman, B., Forveille, T., & Kastner, J. H. 1995, Nature, 373, 494
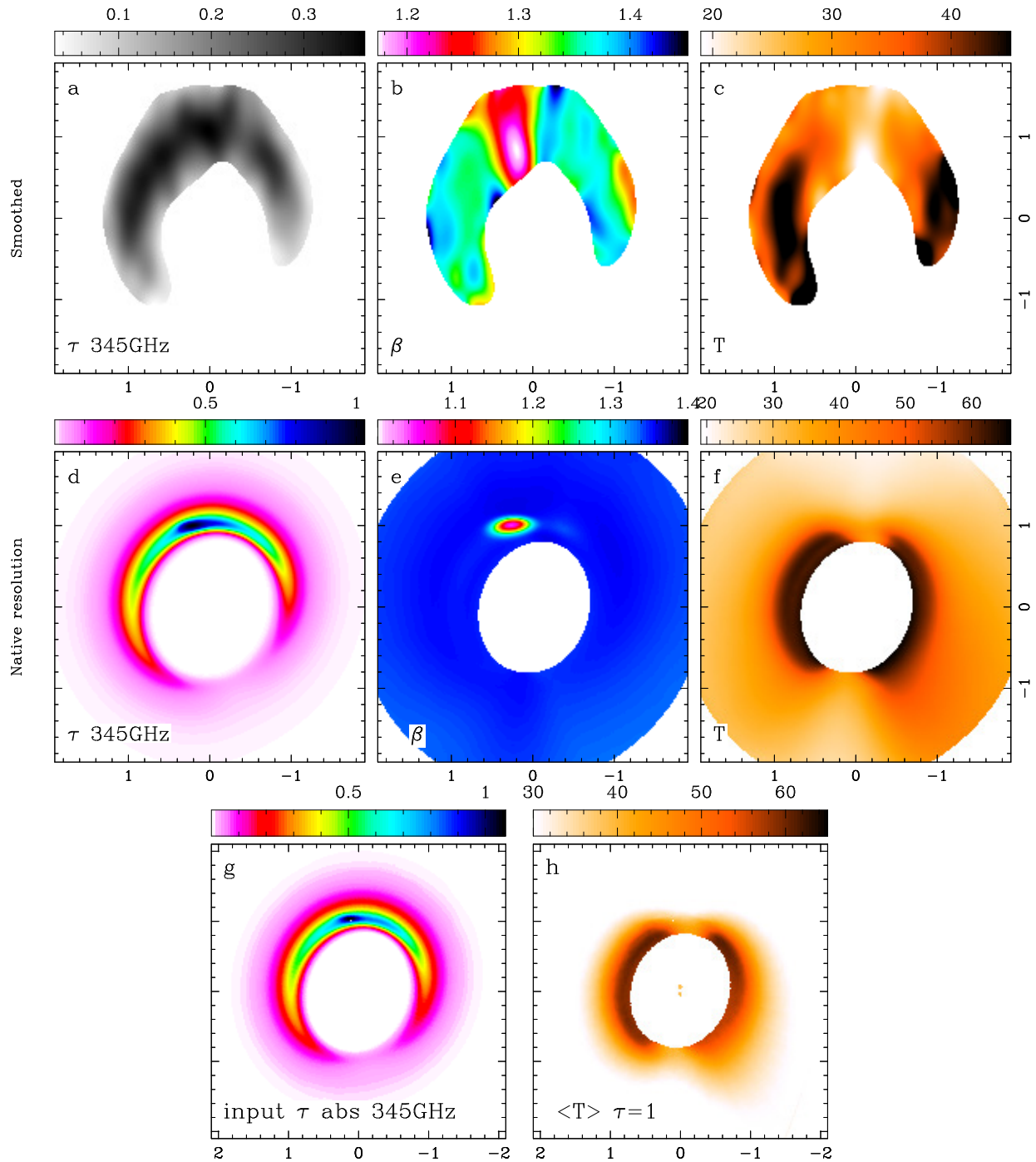
**Figure 13.** Grey-body 'line-of-sight' diagnostics calculated on the radiative transfer predictions, and comparison with input optical depth and temperatures. A mask has been applied to compute line-of-sight diagnostics at a fraction of 1/5 times peak intensity. **a), b), c)**: grey-body diagnostics calculated after filtering by the ATCA+**uvmem** response - **a)** shows the optical depth map at the reference frequency of 345 GHz, **b)** shows the line of sight emissivity index map $\beta_s(\vec{x})$, and **c)** shows line of sight temperature, $T_s(\vec{x})$. **d), e), f)**: same quantities, as calculated on the radiative transfer predictions. **g), h)**: optical depth and average temperature maps used as input for the ray-tracing. See text for the definition of average temperature.